POLITECNICO DI TORINO
Repository ISTITUZIONALE

4D printing of semi-crystalline crosslinked polymer networks with two-way shape-memory effect

Original
4D printing of semi-crystalline crosslinked polymer networks with two-way shape-memory effect / Bonetti, L., Natali, D., Pandini, S., Messori, M., Toselli, M., Scalet, G.. - In: MATERIALS & DESIGN. - ISSN 0264-1275. - 238:(2024). [10.1016/j.matdes.2024.112725]

Availability:
This version is available at: 11583/2995649 since: 2024-12-19T09:47:25Z

Publisher:
Elsevier

Published
DOI:10.1016/j.matdes.2024.112725

Terms of use:

This article is made available under terms and conditions as specified in the corresponding bibliographic description in the repository

Publisher copyright

(Article begins on next page)

02 July 2026

Materials & Design 238 (2024) 112725

Contents lists available at ScienceDirect

Materials & Design

journal homepage: www.elsevier.com/locate/matdes

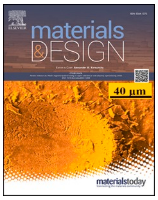

4D printing of semi-crystalline crosslinked polymer networks with two-way shape-memory effect

Lorenzo Bonetti [a,*], Daniele Natali [b], Stefano Pandini [c], Massimo Messori [d], Maurizio Toselli [b], Giulia Scalet [a]

[a] Department of Civil Engineering and Architecture, University of Pavia, Via Ferrata 3, Pavia 27100, Italy
[b] Department of Industrial Chemistry "Toso Montanari", University of Bologna, Viale Risorgimento 4, Bologna 40136, Italy
[c] Department of Mechanical and Industrial Engineering, University of Brescia, Via Branze 38, Brescia 25133, Italy
[d] Department of Applied Science and Technology, Politecnico di Torino, Corso Duca degli Abruzzi 24, Torino 10129, Italy

ARTICLE INFO

Keywords:
Two-way shape-memory polymers
4D printing
Extrusion-based printing
Semi-crystalline crosslinked polymer networks

ABSTRACT

This paper introduces a novel approach to 4D printing tailored structures with reversible two-way shape-memory effect (SME) through material extrusion technology. To this aim, methacrylated poly(ε-caprolactone) (PCL) was synthesized and evaluated from a rheological perspective to determine its suitability for extrusion-based printing. Following a printability assessment, an optimal set of parameters was identified to fabricate 3D structures, UV-crosslinked during printing. Subsequently, a physical and thermo-mechanical characterization of the printed structures was conducted to deepen the understanding of the fabrication process and properties of the obtained structures. To assess the shape-memory properties of the printed structures, both the one-way and two-way SME under load were investigated. Overall, this study opens the floodgates to implementing 4D printing via material extrusion technology, specifically targeting PCL-based semi-crystalline chemically crosslinked polymer networks with two-way SME. Because of its cost-effectiveness, versatility, and user-friendly nature, extrusion-based printing offers noteworthy advantages over other additive manufacturing approaches when reversible behavior of the printed structures is needed. Lastly, a glimpse of potential 4D printed structures from PCL-based semi-crystalline chemically crosslinked polymer networks is presented. The approach described holds significant promise across multiple research and industrial domains, including but not limited to smart actuators, soft robotics, and medical devices.

1. Introduction

Shape-memory polymers (SMPs) are materials able to respond to external stimuli (*e.g.*, heat, light, or magnetic fields) by recovering a permanent shape from one or more programmed temporary shapes, in a phenomenon known as shape-memory effect (SME). In this framework, SMPs have garnered attention due to their remarkable properties, including viability, low-costs, easy tunability, lightweight nature, synthetic flexibility, and biocompatibility [1,2]. Such properties have generated considerable interest across a wide range of applications, spanning from biomedical and pharmaceutical sectors [3] to applications in the aerospace industry [4].

Among the available SMEs, the thermally triggered one-way SME is the most studied. This effect is ensured by a proper combination of the polymer macromolecular structure and the applied thermo-mechanical history, also referred to as shape-memory cycle, and is strictly dependent on the transition temperature (*e.g.*, glass transition or melting temperature) of the polymer used. However, it is worth noting how the non-reversible nature of the one-way SME requires 'reprogramming' the temporary shape from the recovered permanent shape by means of an external thermo-mechanical process. Consequently, the one-way SME may not be suitable for applications where a reversible behavior is demanded, as in the fields of soft actuators and robotics.

Conversely, the thermally triggered two-way SME enables reversibility between two configurations through a cooling-heating cycle. Existing research [4–9] has primarily focused on investigating the two-way SME in liquid crystal elastomers (LCEs) and semi-crystalline crosslinked polymer networks. More recently, it has been demonstrated that the two-way SME can also be achieved without any external applied stress, suggesting the possibility of stress-free (*i.e.*, self-standing)

---

* Corresponding author.
E-mail address: lorenzo.bonetti@unipv.it (L. Bonetti).

https://doi.org/10.1016/j.matdes.2024.112725
Received 21 October 2023; Received in revised form 26 January 2024; Accepted 29 January 2024
Available online 2 February 2024
0264-1275/© 2024 The Author(s). Published by Elsevier Ltd. This is an open access article under the CC BY license (http://creativecommons.org/licenses/by/4.0/).

reversible actuation [4,7,8,10].

SMPs are generally manufactured via traditional fabrication techniques, such as extrusion, injection molding, casting, or subtractive manufacturing [4,11–13]. However, such techniques often demand manual intervention, post-processing, time-consuming processing for assembly, and the fabrication of complex structures is often prevented. To overcome the limitations of traditional fabrication techniques, researchers have delved into alternative methods to streamline the production of complex and/or three-dimensional structures, with 3D printing being a notable example [4,14,15].

3D printing technology has come to the limelight as an advanced technological tool with the pioneering possibility to fabricate objects and structures in a layer-by-layer fashion, enabling the additive production of complex or customized designs that are otherwise challenging to achieve through traditional manufacturing techniques. Nowadays, 3D printing holds a pivotal position in several research fields, among which an attractive line concerns the fabrication of stimuli-responsive structures, *i.e.*, capable of responding to the surrounding environment in a programmed way. This technology is commonly referred as 4D printing, where time represents the 4th dimension and is responsible for the shape evolution of the 3D printed structure [14]. In particular, the integration of SMPs with 4D printing has opened significant opportunities across many application fields.

Over the last few years, several 3D printing techniques have been employed for one-way SMPs, including extrusion-based approaches such as fused filament fabrication (FFF) [16–21] and direct ink writing (DIW) [22–25], vat polymerization approaches such as stereolithography (SLA) [26] and digital light processing (DLP) [27–34], and material jetting approaches such as PolyJet^{TM} technology [35,36]. More recently, FFF [37,38] and SLA [39–41] techniques have also been used to print multiple SMPs.

However, the SMPs used in 4D printing are generally studied only for their one-way SME, thus significantly limiting the breadth of their possible applications.

Li et al. [42] recently shed light on the possibility to 4D fabricate structures with reversible two-way shape-memory behavior via selective laser sintering (SLS) technology, using novel thermoplastic polyamide elastomers. Chalissery et al. [43] disclosed the possibility of using poly (1,10-decylene adipate) (PDA)-based poly(ester urethane) PEU (*i.e.*, a physically crosslinked SMP) in FFF-based 4D fabrication. In addition, structures with two-way SME have been 4D fabricated via DIW technology [44,45], exploiting the shape-memory behavior of LCEs, well known for their large, reversible, and anisotropic shape changes in response to different external stimuli (*e.g.*, temperature and light) [46]. Interestingly, extrusion-based printing offers distinctive advantages over other additive manufacturing technologies (*e.g.*, SLS, DLP, SLA), such as technological low-costs, relative ease of use, versatility, and low materials wastage [47,48].

Despite these latter contributions, to these authors' best knowledge, no works have been found in the literature on extrusion-based 4D fabrication of structures with reversible two-way SME using semi-crystalline chemically crosslinked polymer networks.

To tackle this challenge, we selected polycaprolactone (PCL) semi-crystalline networks, a class of biodegradable SMPs that satisfy essential requirements for their applications as biomedical devices, such as good biocompatibility, biodegradability, ease of chemical modification, fast recovery of large temporary shape configurations, and easy tailoring of their transformation temperatures [49,50]. In particular, methacrylated poly(ε-caprolactone) was synthesized and characterized from a rheological point of view to assess its suitability for printing via fused particle fabrication (FPF), an extrusion-based printing approach [51]. By means of a printability characterization, an optimal set of parameters was identified and selected to fabricate 3D specimens, achieving crosslinking through UV light (365 nm) exposure directly during the printing process. A thorough physical and thermo-mechanical characterization of the 3D printed specimens was then carried out to deepen the knowledge of the fabrication process and products and set the way to the 4D printing through material extrusion technology of structures with two-way SME. The shape-memory properties of the printed specimens were then assessed, investigating both the one-way and two-way SME under stress as a function of different initial levels of pre-strain. Lastly, an overview of some possible 4D printed structures that can be obtained with this technology is drawn, displaying their potential for several research and industrial fields (*e.g.*, smart actuators, soft robotics, and medical devices).

2. Materials and methods

For sake of clarity, a scheme of the work is represented in Fig. 1.

2.1. Materials

High molecular weight PCL ($M_n \sim$ 70–90 kDa), PCL diol (α,ω-hydroxyl-terminated PCL, $M_n \sim$ 10 kDa), 2-isocyanatoethyl methacrylate (2-IEM, 98 %), tin(II) 2-ethylhexanoate, and tetrahydrofuran (THF) were purchased from Merck and used without any further purification step. The photoinitiator, 2-hydroxy-2-methyl-1-phenylpropanone (ADDITOL HDMAP) was purchased from Cytec. In the following, PCL ($M_n \sim$ 70–90 kDa) and PCL diol ($M_n \sim$ 10 kDa) are denoted as PCL70-90 and PCL10, respectively.

2.2. Synthesis of methacrylated PCL (PCL10-MA) and photoinitiator dispersion

PCL10 is a linear hydroxyl-terminated polyester with a number-average molecular weight of 10 kDa, which retains a crystalline phase after forming a crosslinked network [52]. We prepared photo-crosslinkable PCL by adding terminal methacrylate groups. Each hydroxyl-terminated PCL chain can receive up to two methacrylate end groups. The degree of methacrylation determined by ^{1}H NMR spectroscopy [52] was found to be > 98 %. The methacrylation of the hydroxyl end groups of PCL10 with 2-IEM was conducted according to the protocol previously reported [7]. Briefly, dried PCL10 and 2-IEM were introduced into a glass flask in a 1:2.4 M ratio. The reactions were carried out in bulk at 100 °C for about 3–4 h under a nitrogen atmosphere and mechanical stirring. The reaction was monitored by FT-IR until the ratio of peak strength at 2930 and 2275 cm^{-1} became constant. 2-IEM was added with a 20 % stoichiometric excess with respect to hydroxyl groups of the PCL. Unreacted 2-IEM was removed at 100 °C by dynamic vacuum at the end of the reaction, and infrared spectroscopy was performed to ensure the absence of 2-IEM, which is confirmed by the lack of the signal corresponding to the isocyanate group at 2275 cm^{-1}. Further details about the preparation and chemical characterization of these materials can be found elsewhere [52]. Photo-crosslinkable PCL was prepared by melt-mixing at 80 °C (100 rpm, 30 min) the PCL10-MA with the radical photoinitiator (ADDITOL HDMAP, 0.5 wt%). The well-mixed melt was cooled to room temperature (RT), then kept in the dark at RT until use.

2.3. Rheological characterization

The rheological properties of PCL10 and PCL70-90 were investigated to identify the optimal printing conditions. Rheological tests were carried out using a rheometer (Discovery HR 10, TA Instruments) equipped with parallel plate geometry (ϕ = 25 mm, working gap 1 mm). The viscosity of the samples was measured via shear rate sweep tests, by applying a shear rate ($\dot{\gamma}$) ramp in the 0.01–1000 s^{-1} range at different temperatures (T = 70, 80, 90 °C).

2.4. 3D printing

Computer-aided design (CAD) models were drawn in Fusion 360

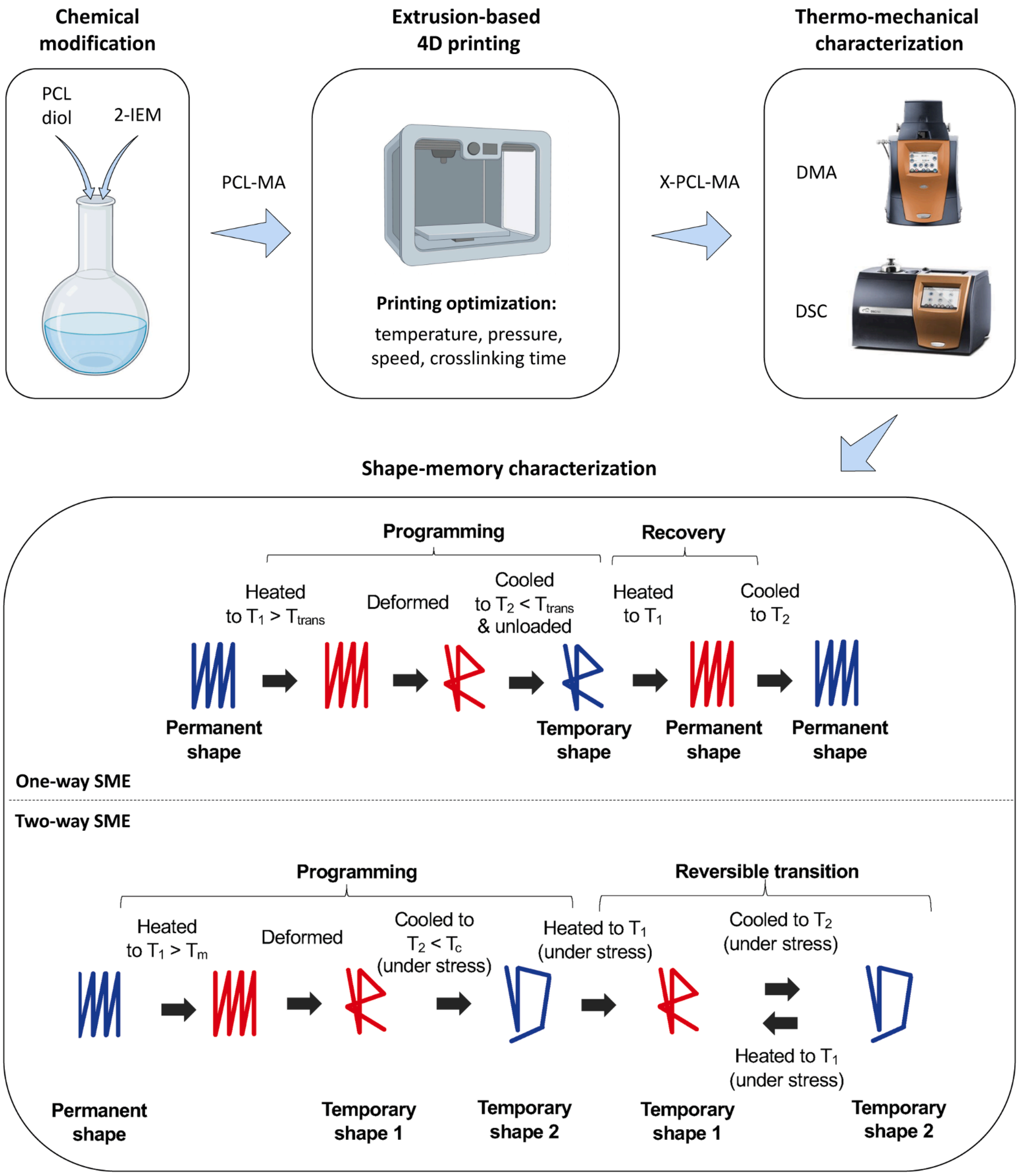

Fig. 1. Scheme of the work: preparation, fabrication, thermo-mechanical, and shape-memory characterization steps. Partially re-adapted from [4].

software (v. 2.0.17457, Autodesk) and processed to obtain .stl files, then imported into DNA Studio (v. 4) software for printing. A pneumatic bioprinter (Cellink BioX6) equipped with a thermoplastic printhead (22 G (0.41 mm) nozzle size, Cellink) was used for printing. The previously prepared PCL10-MA/ADDITOL HDMAP mix was grinded and loaded into the cartridge (10 mL) of the thermoplastic printhead. The printing temperature was set at 70 °C based on rheological data, while the print bed temperature was set at 20 °C. Photo-crosslinking was achieved using the integrated UV module ($\lambda = 365$ nm) of the 3D printer, irradiating each printed layer for 120 s (distance = 6 mm, I = 0.5 mW/cm^2) after extrusion. The crosslinking time (120 s) was selected after an optimization step and represents the plateau in the gel content (G (%)) values (Eq. (4) and Table S1, Supplementary Information). Further irradiation (*i.e.*, 300 s) did not lead to increased G (%) values. For the sake of clarity, non-crosslinked and UV-crosslinked 3D printed samples will be hereafter referred as PCL10-MA and X-PCL10-MA, respectively.

A printability characterization was then carried out to identify optimal printing parameters, as follows (Sections 2.4.1, 2.4.2, 2.4.3).

2.4.1. *Spreading ratio*

Three straight lines (20 x 0.41 x 0.41 mm) were extruded with a printing pressure of 15 kPa and different printing speeds (v = 5–20 mm/s) at 70 °C. Images were acquired with a digital camera (Canon EOS R10) and ImageJ software (v. 1.53) was used to measure the width of the printed strands. The spreading ratio was calculated as follows (Eq. (1)) [53]:

$$Spreading\ ratio = \frac{w_i}{w_0} \tag{1}$$

where w_i and w_0 represent the measured and the CAD-designed widths, respectively. The width measurements were carried out on 5 points for each of the three printed lines, and the w_i calculated as the mean of 15 measures.

2.4.2. *Printing accuracy*

Two concentric squares (l = 10 and 5 mm) were extruded with a printing pressure of 15 kPa, a printing speed of 10 mm/s (identified from spreading ratio tests), and a printing temperature of 70 °C. An image was then acquired and the area of the inner and the outer squares measured. The printing accuracy (%) was calculated as follows (Eq. (2)) [54]:

$$\mathit{Printing\ accuracy}\ (\%) = \left[1 - \left(\frac{|A_i - A|}{A}\right)\right] \times 100 \tag{2}$$

where A_i and A represent the measured and CAD-designed areas, respectively. A_i was calculated as the mean of the inner and outer squares.

2.4.3. Uniformity factor

The uniformity factor was then investigated by printing a 3 × 4 grid (printing conditions: speed = 10 mm/s, pressure = 15 kPa, and printhead temperature = 70 °C). An image was then acquired and the perimeter and area of the six pores was measured. The uniformity factor (Pr) was obtained as follows (Eq. (3)) [55,56]:

$$Pr = \frac{P^2}{16 \times A} \tag{3}$$

where P and A represent the means of the measured perimeter and area, respectively. The Pr parameter was used to determine how well the printed pores matched the CAD-designed ones.

2.5. Characterization

For the following characterizations, rectangular (30 x 5 x 0.41 mm) X-PCL10-MA specimens were fabricated as reported in Section. 2.4.

2.5.1. Gel content

3D printed X-PCL10-MA were characterized in terms of gel content. The specimens were initially weighted (w_0), then placed in THF (immersion ratio = 0.5 $g_{PCL\text{-}MA}$: 15 mL_{THF}) at RT for 24 h. The swollen specimens were then removed from the solvent and dried at RT until a constant weight was achieved, in order to determine the residual weight after extraction (w_d). The gel content (G (%)) were calculated as follows (Eq. (4)) [40]:

$$G(\%) = \frac{w_d}{w_0} \times 100 \tag{4}$$

2.5.2. Thermal characterization

The thermal properties of the specimens were investigated by Differential Scanning Calorimetry (DSC 250, TA Instruments), working between −20 and 100 °C, at 10 °C/min rate, applying heating/cooling/heating scans. The melting (T_m) and crystallization (T_c) temperatures were determined at the local maximum of the endothermic peak and at the local minimum of the and exothermic peak, respectively. The crystallinity content was calculated as follows (Eq. (5)):

$$\chi_c(\%) = \frac{\Delta H_m}{\Delta H_m^{100}} \frac{1}{w_i} \times 100 \tag{5}$$

where ΔH_m is the melting enthalpy of PCL10-MA or X-PCL10-MA in the second heating scan, ΔH_m^{100} is the specific melting enthalpy for a 100 % crystalline PCL (*i.e.*, equal to 139.5 J/g [57]), and w_i is the weight percentage of caprolactone structural units in the polymer.

2.5.3. Thermo-mechanical characterization

The mechanical characterization of the printed specimens was carried out using a Dynamic Mechanical Analyzer (DMA Q850, TA Instruments), in the tensile configuration.

First, quasi-static (QS) tensile tests were performed at 80 °C (*i.e.*, $T > T_m$) by applying a load ramp of 1 N/min (0.001 N preload) up to 18 N (*i.e.*, load limit of the instrument). The Young's modulus (E) was calculated from the slope of the stress–strain curves in the 0–5 % strain range ($R^2 > 0.9$).

Then, the viscoelastic spectrum of the specimens was investigated by applying an oscillating displacement (amplitude = 15 μm, frequency = 1 Hz) under a cooling-heating cycle between 80 and −20 °C at 2 °C/min rate.

2.5.4. Shape-memory characterization

The SME of the specimens was investigated under two different testing protocols.

One-way SME

After an initial preconditioning step (10 min, T = 80 °C, preload = 0.001 N), a load ramp of 1 N/min was applied at 80 °C until a total strain ε = 20 % was reached. Then, a cooling step was performed at 2 °C/min down to −20 °C (*i.e.*, $T < T_c$) keeping the strain fixed (ε = 20 %). Next, the specimen was unloaded (F = 0.001 N) and heated under quasi-stress-free conditions at a constant heating rate of 2 °C/min up to 80 °C.

The ability of the material to be set in a temporary shape was quantified in terms of strain fixity rate (R_f), evaluated as follows (Eq. (6)) [58]:

$$R_f(\%) = \frac{\varepsilon_{unload}}{\varepsilon_{appl}} \times 100 \tag{6}$$

where ε_{appl} represents the nominal strain applied before unloading and ε_{unload} the strain after load removal.

The ability of the material to recover its permanent shape after the quasi-stress-free heating ramp was quantified in terms of strain recovery rate (R_r), evaluated as follows (Eq. (7)) [58]:

$$R_r(\%) = \frac{\varepsilon_{appl} - \varepsilon_{rec}}{\varepsilon_{appl} - \varepsilon_0} \times 100 \tag{7}$$

where ε_{rec} represents the residual strain measured after the heating ramp and ε_0 the strain before initial deformation.

Two-way SME

After an initial preconditioning step (10 min, T = 80 °C, preload = 0.001 N), a load ramp of 1 N/min was applied at 80 °C until a selected strain value (ε = 40 or 50 %) was reached. Then, three cooling-heating cycles between −20 and 80 °C (2 °C/min rate) were carried out under fixed force conditions (corresponding to the level of strain achieved in the previous step).

Two parameters were calculated to quantitatively characterize the two-way shape-memory behavior: the actuation magnitude (AM) and the recovery magnitude (RM), defined by Eqs. (8) and (9), respectively.

$$AM(\%) = \varepsilon_{low} - \varepsilon_{appl} \tag{8}$$

$$RM(\%) = \frac{\varepsilon_{low} - \varepsilon_{high}}{\varepsilon_{low} - \varepsilon_{appl}} \times 100 \tag{9}$$

In the above-reported equations, ε_{appl} represents the strain applied at 80 °C (40 or 50 % nominal), ε_{low} the strain after cooling under load at −20 °C, and ε_{high} the recovered strain at the end of the following heating under load at 80 °C.

2.6. 4D printed structures

The one-way and two-way (under stress) shape-memory response was also evaluated on *ad hoc* specimens drawn in Fusion 360 software (v. 2.0.17457, Autodesk) and processed to obtain .stl files, then imported into DNA Studio (v. 4) software for printing (Cellink BioX6). As can be seen from Table 1 and Fig. 7, five types of samples were designed and fabricated following a 4D printing approach: (1) auxetic structure, (2) gripper, (3) porous structure, (4) actuator, and (5) porous actuator. Such structures were designed to provide an overview of some potential applications of 4D printing via material extrusion technology.

The thermal-triggered evolution over time (4th dimension in the "4D printing" definition) of these specimens was explored by first heating them at about 80 °C, deforming them in a temporary configuration, and fixing the configuration by cooling them at about 4 °C. Then, the one-

Table 1
4D printed X-PCL10-MA specimens. Both one-way and two-way (under stress) SMEs were evaluated. 2D = monolayer, 3D = multiple layers.

Specimen type	SME	2D/3D
Auxetic structure	One-way	2D
Gripper	One-way	3D
Porous structure	One-way	3D
Actuator	Two-way	2D
Porous actuator	Two-way	3D

way SME was investigated, subjecting the specimens to isothermal recovery test by immersion into a hot water bath (T = 80 °C). The recovery process was monitored from images and videos by means of a digital camera (Canon EOS R10). The two-way SME was investigated by subjecting the specimen to heating/cooling cycles under load, by moving them between two beakers containing water at 80 and 4 °C. Specifically, the load (80 g) was selected according to quasi-static tensile tests (Section 2.5.3) to achieve a strain value of about 40 % at the programming temperature (80 °C). The actuation magnitude (AM) was calculated as follows (Eq. (10)):

$$AM(\%) = \varepsilon_{4^\circ C} - \varepsilon_{80^\circ C} \tag{10}$$

where $\varepsilon_{4^\circ C}$ and $\varepsilon_{80^\circ C}$ are the strain at 4 and 80 °C, respectively.

Images and videos were acquired with a digital camera (Canon EOS R10).

3. Results and discussion

3.1. Printing optimization

PCL70-90 was selected as a reference material, as already reported in the literature for extrusion-based printers. In this regard, a temperature range of 70–135 °C has been reported for the 3D printing of PCL70-90, depending on the printing parameters (*e.g.*, nozzle diameter, printing speed, printing pressure) [59–61]. In this work, T = 90 °C was selected as optimal for PCL70-90 3D printing based on a preliminary printing optimization (data not shown).

The viscosity of PCL10 and PCL70-90 as a function of temperature (Fig. 2) was investigated to identify the optimal printing temperature for PCL10. As it is possible to observe in Fig. 2, PCL10 viscosity increased by decreasing the temperature in the range from 90 to 70 °C. In particular, a T = 70 °C led to viscosity values close to the ones of PCL70-90 at 90 °C, suggesting that a suitable temperature for PCL10 printing must be equal or close to 70 °C.

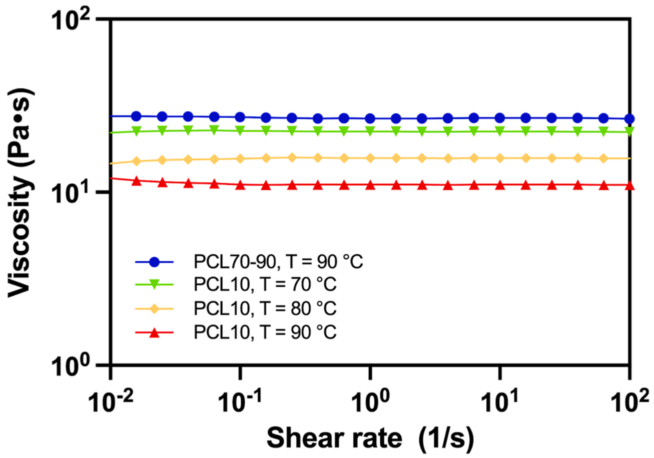

Fig. 2. Representative viscosity (η) *vs.* shear rate ($\dot{\gamma}$) curves for PCL10 and PCL70-90.

Fused particle fabrication (FPF) -or fused granular fabrication (FGF)- was the additive manufacturing technique here exploited. FPF is an extrusion-based printing approach that offers the advantage of bypassing the melting/extrusion/crystallization cycle used in FFF to obtain the printing filament; in fact, printing via FPF is achieved directly from pellets, flakes, or regrind [51].

A first printability test was carried out on PCL10-MA to identify a suitable printing pressure and assess the formation of a uniform strand following extrusion [62]. A pressure (P) of 15 kPa was found as optimal and selected for further printability characterization.

The spreading ratio (Fig. 3A) was calculated from Eq. (1) by varying the printing speeds in the 5–20 mm/s range (P = 15 kPa, T = 70 °C). Values close to 1 indicate a good fit between the printed and the CAD-designed strand diameter [55]. Following this approach, a printing speed of 10 mm/s led to a spreading ratio of 1.01 ± 0.05 and was thus selected as optimal.

Moreover, using the optimized set of printing parameters (P = 15 kPa, v = 10 mm/s, T = 70 °C), the printing accuracy (Fig. 3B), calculated from Eq. (2), reached values of 97.7 ± 1.9 %; the uniformity factor (Fig. 3C), calculated from Eq. (3), resulted close to 1 (Pr = 0.98).

Overall, such outcomes indicate the achievement of optimally printed structures with good shape fidelity [55]. Using the optimized set of printing parameters, three-dimensional X-PCL10-MA samples (30 x 5 x 0.41 mm) were printed for further characterizations (Fig. 3D). The printing process was carried out by setting the print bed temperature at 20 °C, to allow a fast crystallization of the PCL10-MA (T_c = 29 °C, Section 3.2) and to achieve good shape fidelity [63]. Following extrusion, photo-crosslinking was achieved directly in the 3D printer, using the integrated UV module at λ = 365 nm.

3.2. Thermal and physical properties of the 3D printed samples

The thermal properties of the 3D printed X-PCL10-MA specimens were analyzed by DSC (Fig. 4) and compared with PCL10-MA not subjected to any UV irradiation (Table 2). X-PCL10-MA showed a melting temperature (T_m) of 52 °C and a crystallization temperature (T_c) of 26 °C, comparable to that of PCL10-MA.

However, different χ_c values (Eq. (5)) were found: 40 *vs.* 57 % for UV-crosslinked and non-crosslinked samples, respectively (Table 2). Such a reduction in the crystallinity content after crosslinking can be ascribed to a hindered crystallization process, due to the restricted chain mobility in the presence of chemical net points [64]. These data deviate from our previously reported work on UV-crosslinked PCL10-based networks [7], presenting lower transition temperatures and crystalline fractions (T_m = 42 °C, T_c = 8 °C, χ_c = 30 %). A possible explanation for the absence of shifts in the transition temperatures for the crosslinked samples probably lies in the temperature at which the UV crosslinking step is carried out: in the present work, such a temperature was lower than the one used in our previous investigation (20 *vs.* 80 °C). Crosslinking temperature must thus be regarded as a critical factor in modulating the thermal properties of crosslinked PCL. On this topic, similar outcomes have been reported on photo-cured epoxy/PCL blends, where PCL crosslinking reaction at room temperature (*i.e.*, T < T_c) was reported to take place in the amorphous regions of PCL [63].

The achievement of an efficient crosslinked structure through the UV curing process is however evidenced by the gel content of the samples (G ~ 85 %, Table 2), calculated from Eq. (4), revealing the presence of a high insoluble PCL fraction. Such results are comparable or slightly lower than our previous works, where G values in the 90–94 % range were found for UV-crosslinked PCL10-PEG semi-crystalline networks [7] and PCL10 crosslinked by sol–gel chemistry [50].

3.3. Thermo-mechanical properties of the 3D printed samples

Quasi-static tensile tests were carried out on X-PCL10-MA samples at 80 °C, that is, above their T_m. Fig. 5A displays a representative stress/strain curve obtained for these tests. As it is possible to observe, the

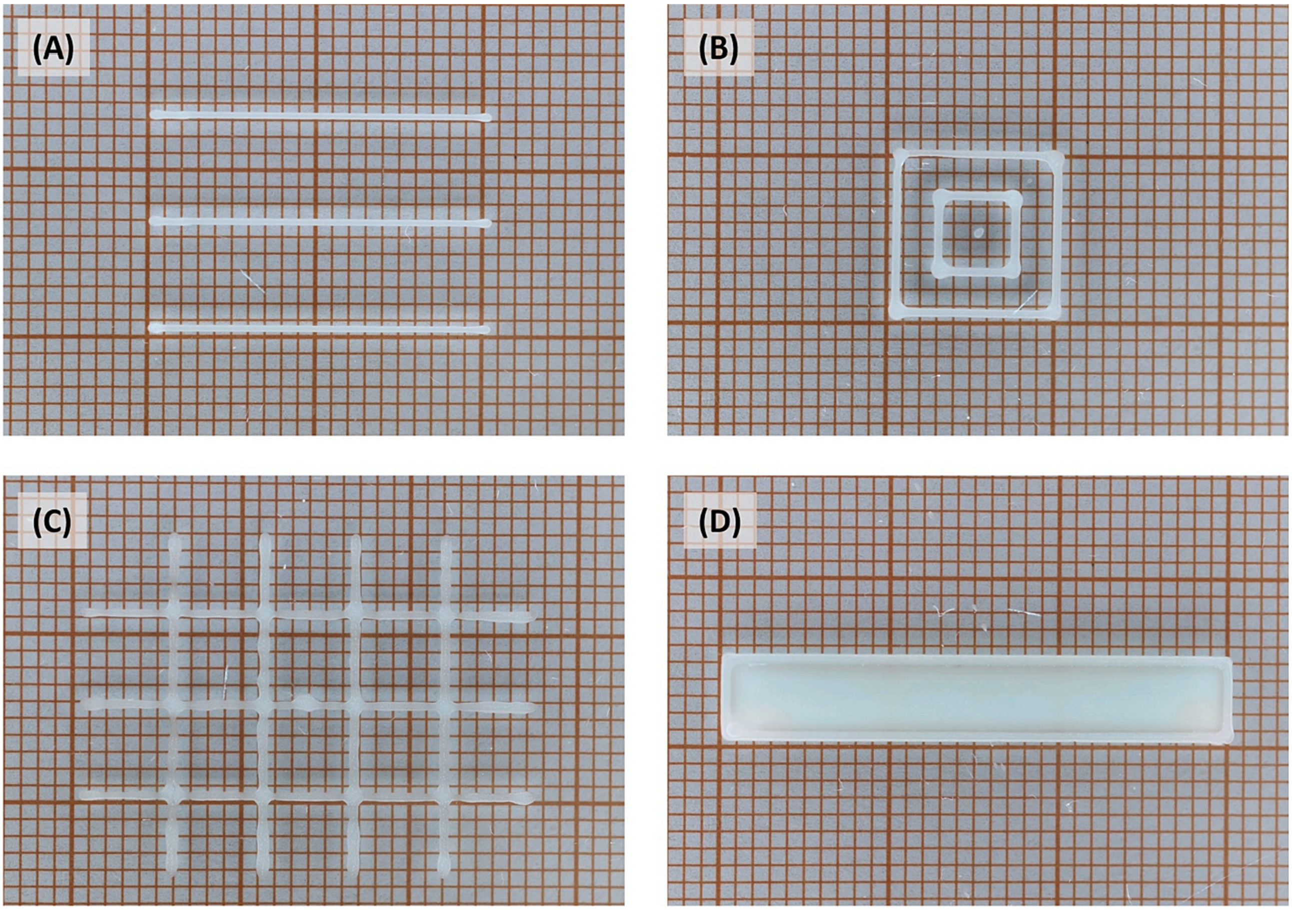

Fig. 3. 3D printing optimization: (A) the spreading ratio was calculated by printing three straight lines (20 x 0.41 x 0.41 mm), (B) the printing accuracy was calculated by printing two concentric squares (l = 10 and 5 mm), and (C) the uniformity factor by extruding a 3 × 4 grid. The optimal printing parameters (T = 70 °C, P = 15 kPa, v = 10 mm/s) were then set to print 30 x 5 x 0.41 mm X-PCL10-MA samples (D), used to assess the thermo-mechanical and shape-memory properties.

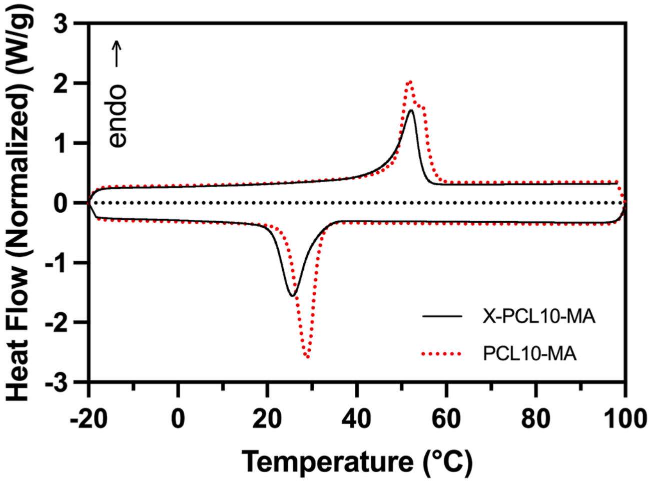

Fig. 4. DSC cooling and second heating scan at 10 °C/min for PCL10-MA and X-PCL10-MA.

specimens did not break within the test window, reaching strain values ε ~ 140 % at the end of the test (corresponding to the displacement limit of the machine). The Young's modulus (E), calculated from the slope of the σ/ε curves, resulted equal to 1.41 ± 0.01 MPa (Table 3).

The crosslinking density (ν) was then calculated from the tensile modulus by applying the statistical Gaussian rubber theory following Eq. (11) [50]:

Table 2
Physical and thermal properties of PCL10-MA and X-PCL10-MA (DSC at 10 °C/min).

Material	UV	T_c (°C)	T_m (°C)	ΔH_m (J/g)	χ_c(%)	G (%)
X-PCL10-MA	Yes	26*	52*	54	40	84.5 ± 0.1
PCL10-MA	No	29	52	77	57	–

[*] NOTE: T_c calculated from onset point = 31 °C, T_m calculated from onset point = 47 °C (useful for comparison with the T_{CIE} and T_{MIC}, please refer to Section 3.4).

$$E = 3\nu RT \tag{11}$$

where E is the Young's modulus, R is the universal gas constant, and T is the absolute temperature.

Both the E and ν values obtained for the 3D printed samples (Table 3) are in line with our previous outcomes on PCL10 semi-crystalline networks chemically crosslinked through sol–gel reaction (E = 2.5 ± 0.2 MPa, $\nu = 1.2 \times 10^{-4}$ mol cm^{-3}) [6,50]. Despite the different crosslinking approaches, the comparable values obtained indicate the achievement of a crosslinked polymer with promising structure and properties for successful shape-memory behavior.

Fig. 5B displays a representative storage modulus (E') *vs.* temperature curve resulting from the DMA characterization of the printed samples. The test was performed starting at T = 80 °C and performing a controlled cooling below the sample's T_c and a subsequent heating above its T_m to characterize both the crystallization and melting phenomena. Upon cooling, the DMA trace displays a marked E' increase

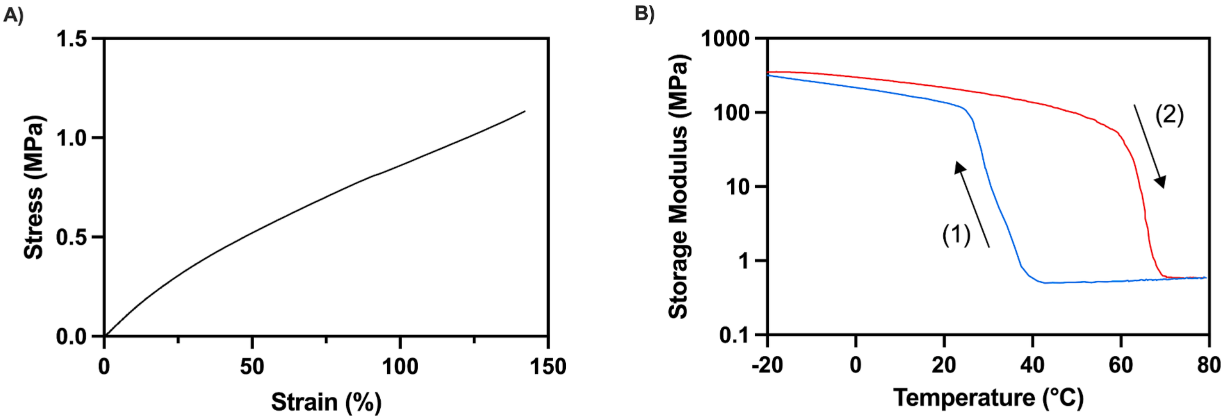

Fig. 5. Thermo-mechanical characterization of 3D printed X-PCL10-MA. Representative A) quasi-static tensile test (T = 80 °C) and B) DMA traces. The blue and red curves represent the cooling (1) and heating (2) steps, respectively. (For interpretation of the references to colour in this figure legend, the reader is referred to the web version of this article.)

Table 3
Material properties derived from QS tensile tests and thermo-mechanical characterization of the 3D printed X-PCL10-MA.

E at 80 °C (MPa)	Crosslinking density ν (10^{-4} mol cm^{-3})	E' at −20 °C (MPa)	E' at 80 °C (MPa)
1.41 ± 0.01	1.60 ± 0.01	337	0.59

around 25–35 °C, that is, near the specimen's T_c, reaching E' values around 300 MPa at −20 °C (Table 3). Upon second heating, the trace displays a noticeable E' drop in a narrow region close to about 65 °C, as previously observed for PCL-based systems [64]. A plateau with E' values around 500 kPa is reached above the melting temperature, confirming the achievement of a crosslinked structure (Table 3) [64].

3.4. Shape-memory characterization

First, the one-way shape-memory behavior of the samples was investigated by applying a defined thermo-mechanical cycle by means of DMA, as depicted in Fig. 6A. The assessment of the one-way shape-memory response consists in fixing a temporary shape, followed by recovery of the permanent shape under a thermal stimulus. The thermo-mechanical cycle starts (1) deforming the specimen up to 20 % tensile strain at 80 °C, then (2) cooling to −20 °C under constant strain (ε = 20 %), (3) setting the force to 0.001 N to unload the sample, and lastly (4) heating up to 80 °C under quasi-stress-free conditions. The heating and cooling rates were set to 2 °C/min. The strain fixity rate (R_f) and the strain recovery rate (R_r) were than calculated according to Eqs. (5) and (6), respectively. The high R_f value (95.5 ± 0.5 %) indicates that the applied strain is almost completely maintained after unloading, suggesting that crystallization occurred efficiently by cooling the sample.

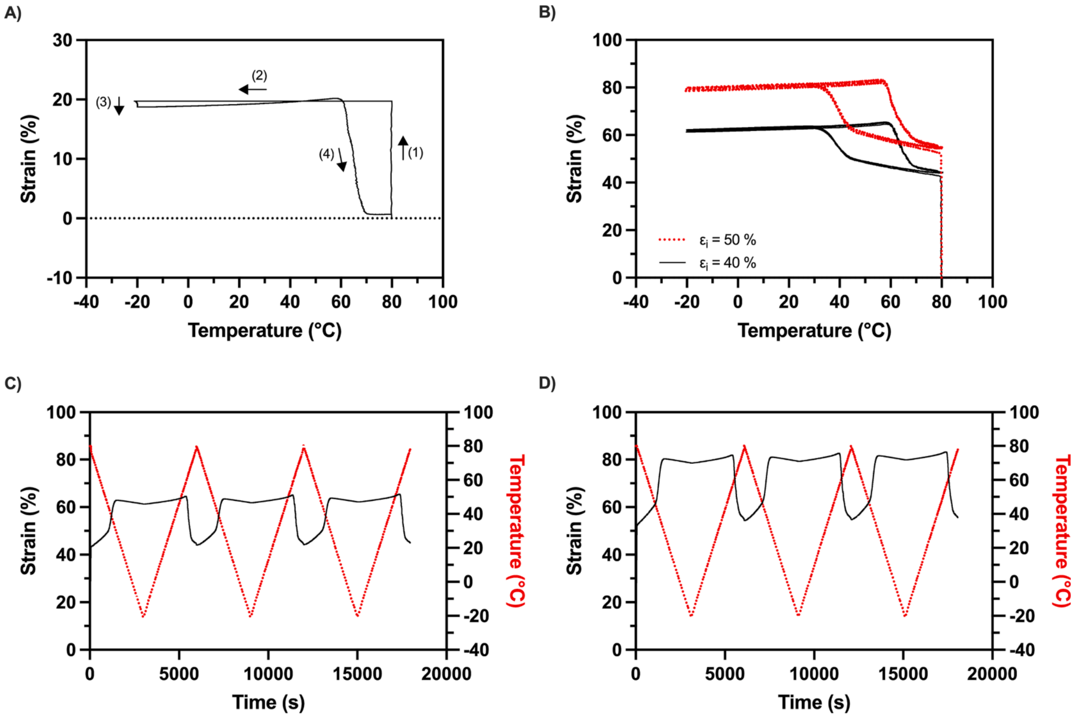

Fig. 6. Shape-memory effect of 3D printed X-PCL10-MA. A) Representative one-way shape-memory test. B) Two-way shape-memory tests at two levels of strain (ε = 40, 50 %) under mechanical load. Three cycles for the two-way shape-memory tests at C) 40 % and D) 50 % strain, in terms of time *vs.* strain (black)/temperature (red) curves. (For interpretation of the references to colour in this figure legend, the reader is referred to the web version of this article.)

Moreover, the high R_r value (95.5 ± 1.4 %) indicates an almost complete recovery of the permanent shape upon heating above T_m [65]. Such data are in good agreement with our previously reported works on PCL-based SMPs (processed by traditional fabrication techniques), where high (>95 %) R_f and R_r values were found [50,65]. This suggests that the printing process does not negatively affect the excellent one-way shape-memory capabilities of the material.

The two-way SME was then investigated to assess the possibility of reversible shape changes in the presence of a mechanical load (Fig. 6B). In fact, two-way thermo-responsive SMPs possess the ability to undergo a reversible change in shape between two different configurations in response to an on–off stimulus [4], in this study represented by a cooling-heating cycle. Similar to the one-way SME, the two-way SME is a result of a suitable combination of the polymer's macromolecular architecture with a specific thermo-mechanical history, represented by the shape-memory cycle.

The two-way SME under constant stress is a characteristic feature exhibited by two classes of SMPs: (i) semi-crystalline crosslinked polymer networks and (ii) LCEs. Achieving two-way SME in semi-crystalline crosslinked polymer networks requires the simultaneous presence of a crystallizable phase and chemical crosslinks. In particular, the two-way SME under constant tensile stress involves the elongation of the polymer network, driven, first, by an entropy elasticity effect in the rubbery region and then by crystallization upon cooling below the crystallization temperature. On the other hand, the contraction of the polymer network occurs during heating above the melting temperature, attributed to the melting of the temporary-oriented crystalline domains. This elongation is termed crystallization-induced elongation (CIE), and the contraction is referred to as melting-induced contraction (MIC) [4].

To assess the two-way SME, a controlled (1 N/min) load ramp at T = 80 °C (*i.e.*, $T > T_m$) was first applied until a selected strain value ($\varepsilon = 40$ or 50 %) was reached. It is worth mentioning that the applied pre-strain was far below the strain at break (ε_b) of the samples (*i.e.*, $\varepsilon_b > 140$ %, Fig. 5A). While holding the force (corresponding to the strain achieved at the end of the previous step) constant, a cooling/heating cycle between −20 °C and 80 °C at a controlled rate (2 °C/min) was carried out to evaluate the reversible strain change resulting from CIE and the subsequent MIC.

In fact, upon cooling, the ε *vs.* T curves display the typical elongation upon cooling, consisting of two processes: an entropy-driven one and a crystallization-driven one [9,50,64,66]. The former occurs for $T > T_c$ and causes an initial slight increase of strain, while the latter appears as a steeper ε increase with crystallization. The temperature at which CIE takes place (T_{CIE}, Table 4) was calculated from the onset point of the steepest elongation process in the ε *vs.* T curve (T_{CIE} was calculated on the first cooling/heating cycle). The T_{CIE} resulted higher than the T_c obtained by DSC (T_c = 31 °C when using the onset point method, Table 2), but this can be due to both the different cooling rate (2 *vs.* 10 °C/min for DMA and DSC, respectively) and to the fact that crystallization with a stress applied is known to occur at higher temperatures due to the favorable alignment of the PCL polymeric chains [7].

Upon heating, the ε *vs.* T curves display the typical contraction process, consisting of two opposed processes: a slight thermal expansion and a sharp melting-induced contraction. The overall effect is a strain reduction, happening as the sum of two subprocesses, finally leading to a strain very close to that displayed before the cooling-heating cycle [7].

Table 4
Two-way shape-memory tests under applied load on 3D printed X-PCL10-MA.

ε (%)	σ (MPa)*	AM (%)	T_{CIE} (°C)	T_{MIC} (°C)	RM (%)
40	0.45	20.6	43	61	80.8
50	0.52	28.7	43	58	82.4

[*] NOTE: σ is the stress reached at the end of the loading phase (and corresponding to the reported strain, ε), then kept constant during the cooling/heating cycles.

Similarly to the calculation of the T_{CIE}, the temperature at which MIC takes place (T_{MIC}, Table 4) was calculated from the onset point of the steepest contraction process in the ε *vs.* T curve (T_{MIC} was calculated on the first cooling/heating cycle). The T_{MIC} resulted higher than the T_m obtained by DSC (T_c = 47 °C when using the onset point method, Table 2), but again this difference can be attributed to the same reasons above-mentioned for CIE.

The actuation and recovery magnitude (AM and RM) were then calculated on the first heating/cooling cycle of the two-way shape-memory tests using Eqs. (7) and (8) (Table 4). The AM values were found to be equal to 20.6 and 28.7 % (for ε = 40 and 50 %, respectively), indicating a good extent of change in strain obtained upon crystallization. Interestingly, the AM was found to increase with the level of pre-strain applied (Fig. 6C and D). In this regard, it is widely recognized that, once a minimum threshold for activating the elongation process during crystallization is exceeded, a higher applied load leads to an increased elongation. This phenomenon may be attributed to a structural evolution within the material during crystal formation, resulting in a progressively higher crystallite orientation along the stretching direction as the applied stress increases [7]. The RM values were found to be equal to 80.8 and 82.4 % (for ε_{appl} = 40 and 50 %, respectively), implying that an efficient recovery process of the deformation was achieved [7] without substantial differences depending on the level of the applied pre-strain.

AM and RM data are in good agreement with our previously reported works on PCL-based SMPs (processed by traditional fabrication techniques), where mean AM and RM values of 26 and 94 % (for σ = 500 kPa, corresponding to ε ~ 40 %) were found [50]. Such outcomes suggest that the printing process did not negatively affect the two-way shape-memory capabilities of the material.

Lastly, it is worth mentioning that a good repeatability was obtained after three heating/cooling cycles. In this regard, a good overlapping in the ε *vs.* T curves was obtained (Fig. 6B), without any loss of performance over the three thermal cycles. Also the three elongation – contraction cycles reported in Fig. 6C and Fig. 6D for the two levels of applied strain highlight such a good repeatability from cycle to cycle.

Overall, the printed specimens displayed outstanding two-way shape-memory behavior under stress, showing substantial elongation – contraction effects when exposed to cooling/heating cycles within the crystallization and melting regions.

3.5. *Performances of the 4D printed structures*

In this section, a selection of 4D printed structures obtained via material extrusion technology is reported, to unveil the potential of this technology in the fabrication of structures featuring both one-way and two-way shape-memory properties.

For all the 4D printed structures, one-way recovery occurred in few seconds at 80 °C, thus the SME was followed by recording a video. For two-way SME under load, the process was followed via image analysis obtained from a digital camera.

Auxetic structure.

An auxetic structure, having a negative Poisson's ratio, can expand transversally when axially elongated under tensional force [39,41]. Here, a 2D re-entrant honeycomb structure with auxetic effect (Fig. 7A) was designed according to what described by Gibson et al. [67,68]. Theoretically, when subjected to vertical directional load (and the diagonal ribs are extended in the vertical direction), its units move in the horizontal direction, consequently leading to an auxetic effect. The sample (Fig. 7A) was first programmed by placing it in hot water (80 °C), deforming it by means of tweezers, and fixing the temporary shape by cooling it in a cool water bath (4 °C). The recovery of the permanent shape was then achieved by immersing the sample in hot water (80 °C) (Video S1, Supplementary Information).

Gripper.

A gripper structure was designed with the purpose of grabbing

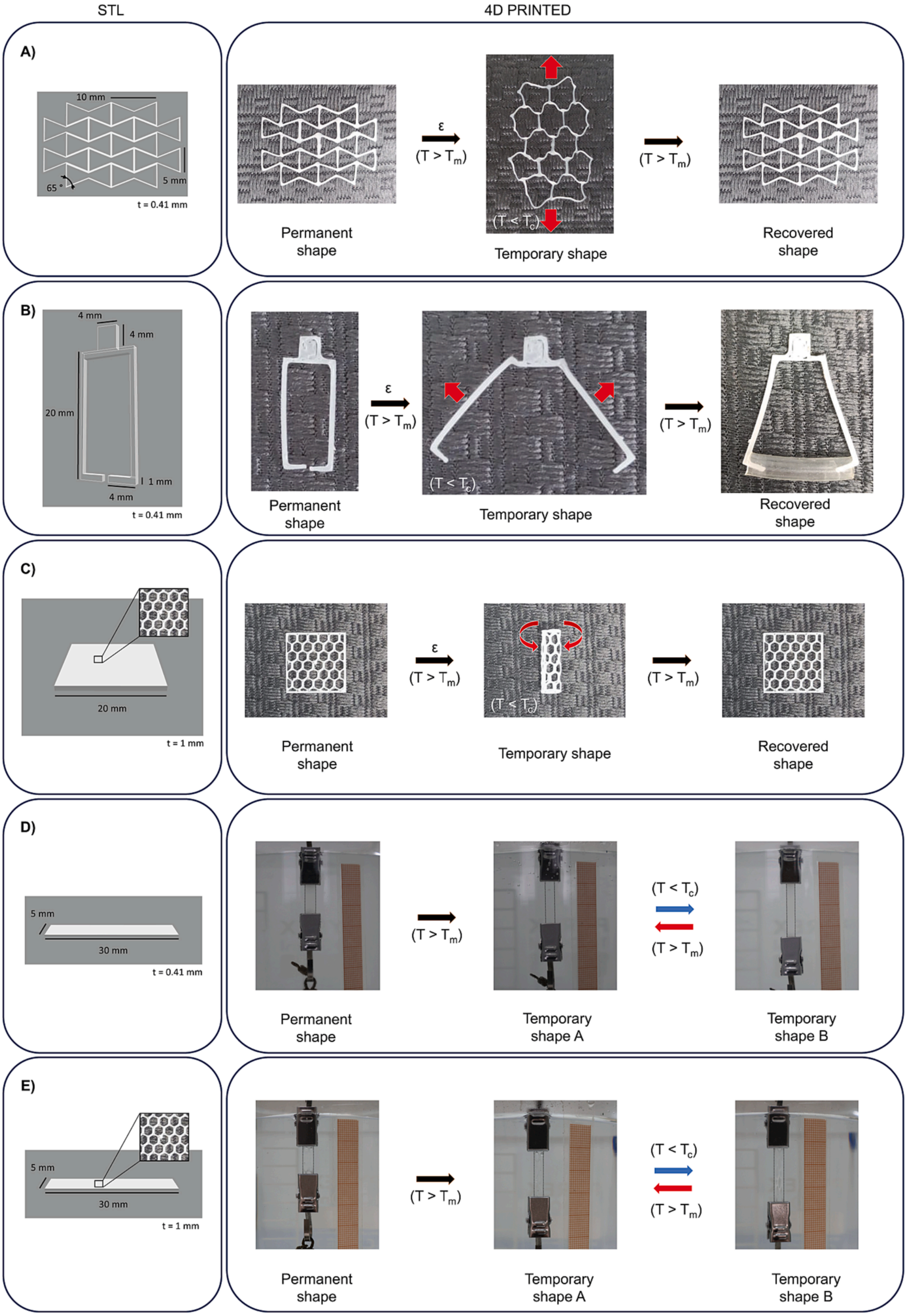

Fig. 7. 4D printed X-PCL10-MA obtained via material extrusion technology. A) Auxetic structure, B) gripper (the recovered shape displays the functionality of grabbing an object, *i.e.*, tube), and C) porous structure (porosity was achieved by selecting a 25 % honeycomb infill directly from the 3D printer software) were investigated for one-way SME. Red arrows indicate the direction of the deformation applied in the programming step. D) Actuator, investigated for two-way SME under load. E) Porous actuator, investigated for two-way SME under load (porosity was achieved by selecting a 25 % honeycomb infill directly from the 3D printer software). Please refer to Figure S1 (Supplementary Information) for the image of the complete set-up (actuator + load). Note: t = thickness of the CAD model. (For interpretation of the references to colour in this figure legend, the reader is referred to the web version of this article.)

objects triggered by a thermal stimulus [69,70]. In Fig. 7B, an as-printed closed gripper was opened (programmed) at 80 °C and fixed by immersion in a cool water bath (4 °C). After programming, the functionality of grabbing objects (tube) was triggered upon heating (80 °C water bath). Fig. 7B displays time-lapsed images of the gripper holding an object (Video S2, Supplementary Information) and proves such a structure as promising for capture work and movement tasks.

Porous structure.

A porous 3D structure (Fig. 7C) was obtained by designing a box geometry (20 x 20 x 1 mm) and selecting a 25 % honeycomb infill directly from the 3D printer software (DNA Studio, v. 4). The as-printed porous structure was wrapped around a metal spindle (programmed) at 80 °C and fixed by immersion in a cool water bath (4 °C). The one-way recovery of the permanent shape was triggered upon immersion in a hot (80 °C) water bath (Video S3, Supplementary Information). Interestingly, it is noteworthy mentioning that the one-way SME was preserved on the 3D structure, even when multiple layers were printed. In this regard, it has been reported the loss of the SME on 3D structures made from photo-cured epoxy/PCL blends even on thin (0.5 mm thickness) samples printed via FFF, ascribed to the poor interlayer adhesion after printing and crosslinking [63]. Conversely to this study, where photo-crosslinking has been achieved after the obtainment of the 3D printed object, in our work photo-crosslinking was achieved in a layer-by-layer fashion directly with the 3D printer's built-in UV source. It can be thus supposed that the crosslinking approach (after the last layer *vs.* layer-by-layer) could significantly impact on the overall shape-memory behavior of the 3D printed structure.

Actuator.

In order to assess the two-way SME under load, a 4D printed specimen (X-PCL10-MA, 30 x 5 x 0.41 mm) was tested with an 80 g weight (Fig. S1, Supplementary Information). The sample was first programmed by placing it in hot water (80 °C), hanging it vertically with an 80 g weight attached at its bottom by means of two metal clips (Fig. 7D). At this stage, the sample reached a strain ($\varepsilon_{80\ ^\circ C}$) of 42.4 %, as expected from quasi-static mechanical tests. The sample was then moved into a cold-water bath (4 °C), and the strain change resulting from the CIE measured. At this stage, the sample reached a strain ($\varepsilon_{4\ ^\circ C}$) of 80.9 %, leading to an AM value of 38.5 %. The AM resulted significantly higher than the corresponding values obtained from DMA tests (20.6 *vs.* 38.5 %, see Section 3.4), but such a difference can be due to the different protocols applied. For DMA tests the specimens were tested in air, at a controlled heating/cooling rate of 2 °C/min, while in the present case the specimen was studied in water, rapidly moving it between water baths at two different temperatures (80 and 4 °C). In this regard, both the presence of a solvent (*e.g.*, water) [71] and the applied temperature ramps [11] have been reported to have an impact on the shape-memory properties of different SMPs. Moreover, possible differences in the applied force (DMA *vs.* 80 g weight) could also have contributed to the shift in AM values. A total of three heating/cooling cycles were applied to the specimen, which displayed reproducible two-way SME.

Porous actuator.

In order to demonstrate the two-way SME under load on a complex shape, a 4D printed specimen (X-PCL10-MA, 30 x 5 x 1 mm) with a 25 % honeycomb infill (DNA Studio, v. 4) was tested with an 80 g weight. The sample was first programmed by placing it in hot water (80 °C), hanging it vertically with an 80 g weight attached at its bottom by means of two metal clips (Fig. 7E). At this stage, the sample reached a strain ($\varepsilon_{80\ ^\circ C}$) of 59 %. The sample was then moved into a cold-water bath (4 °C), and the strain change resulting from the CIE measured. At this stage, the sample reached a strain ($\varepsilon_{4\ ^\circ C}$) of 88.8 %, leading to an AM value of 29.8 %. A total of three heating/cooling cycles were applied to the specimen, which displayed reproducible two-way SME. No DMA characterization was carried out on porous actuators, since such characterization for this particular specimen type was outside of the purposes of this work. (For the quantitative characterization of the two-way SME, please refer to the previous sample type, "Actuator").

4. Conclusions: potentialities, limitations, and possible improvement strategies

Extrusion-based printing has been here established for the first time for the fabrication of structures featuring the two-way shape-memory behavior using semi-crystalline chemically crosslinked polymer networks based on PCL. After an initial printing optimization phase, 3D structures were successfully printed and crosslinked by exposing them to UV light directly during the printing process. The obtained samples displayed good thermo-mechanical properties and excellent shape-memory performance, in terms of one-way and two-way under stress response, with significant elongation-contraction effects when subjected to cooling/heated cycles across the crystallization and melting regions of PCL. Overall, due to the advantages over other additive manufacturing techniques, among which low costs, ease of use, and versatility, extrusion-based printing offers noteworthy advantages for a wide range of potential applications where a reversible behavior of the printed structures is needed.

Such systems lend themselves well for several applications, ranging from smart actuators to soft robotics and personalized stimuli-responsive medical devices (*e.g.*, shape-memory scaffolds and devices). In particular, in the biomedical area shape-memory PCL-based systems have already been reported, for instance for cell culture surfaces [72], tissue engineering (*e.g.*, bone [73], muscle [74]), or drug delivery systems [75]. Thus, the envisaged applications of the structures here reported are countless.

Possible limitations of the developed systems are mainly two, namely (i) the limited cell adhesion and (ii) the limited mechanical properties of PCL.

In this regard, PCL is well recognized as hardly cell adhesive, due to its hydrophobic nature. However, several possible options to tackle this limitation have been identified in the literature, for instance chemical modification with cell adhesive sequences (*e.g.*, RGD peptides [76]), plasma treatment [77], or blending with other polymers (*e.g.*, PLA [78]).

In terms of mechanical properties, a possible limitation consists in the scarce applicability of PCL in load-bearing systems. In this regard chemical crosslinking, blending, or use of inorganic fillers (or combination of them) have been reported in the literature as possible strategies to overcome this limitation [79]. Such approaches, coupled with the fine-tuning of the polymerization (and/or chemical modification), can open up to a plethora of different applications of PCL-based systems, even under harsh mechanical, physical, and chemical conditions without significant loss of their properties [49].

CRediT authorship contribution statement

Lorenzo Bonetti: Conceptualization, Data curation, Formal analysis, Investigation, Methodology, Visualization, Writing – original draft, Writing – review & editing. **Daniele Natali:** Conceptualization, Investigation, Writing – original draft, Writing – review & editing. **Stefano Pandini:** Conceptualization, Methodology, Writing – review & editing. **Massimo Messori:** Conceptualization, Writing – review & editing. **Maurizio Toselli:** Conceptualization, Investigation, Methodology, Writing – original draft, Writing – review & editing. **Giulia Scalet:** Conceptualization, Data curation, Formal analysis, Funding acquisition, Investigation, Methodology, Project administration, Supervision, Visualization, Writing – original draft, Writing – review & editing.

Declaration of competing interest

The authors declare that they have no known competing financial interests or personal relationships that could have appeared to influence the work reported in this paper.

Data availability

Data generated in this study are deposited in the Zenodo database at https://doi.org/10.5281/zenodo.10567550

Acknowledgments

This work was funded by the European Union ERC CoDe4Bio Grant ID 101039467. Views and opinions expressed are however those of the author(s) only and do not necessarily reflect those of the European Union or the European Research Council. Neither the European Union nor the granting authority can be held responsible for them.

Appendix A. Supplementary data

Supplementary data to this article can be found online at https://doi.org/10.1016/j.matdes.2024.112725.

References

[1] A. Lendlein, O.E.C. Gould, Reprogrammable recovery and actuation behaviour of shape-memory polymers, Nat. Rev. Mater. 4 (2019) 116–133, https://doi.org/10.1038/s41578-018-0078-8.

[2] J. Hu, Y. Zhu, H. Huang, J. Lu, Recent advances in shape–memory polymers: Structure, mechanism, functionality, modeling and applications, Prog. Polym. Sci. 37 (2012) 1720–1763, https://doi.org/10.1016/j.progpolymsci.2012.06.001.

[3] Y. Xia, Y. He, F. Zhang, Y. Liu, J. Leng, A review of shape memory polymers and composites: mechanisms, materials, and applications, Adv. Mater. 33 (2021), https://doi.org/10.1002/adma.202000713.

[4] G. Scalet, Two-way and multiple-way shape memory polymers for soft robotics: an overview, Actuators 9 (2020) 10, https://doi.org/10.3390/act9010010.

[5] M. Zare, M.P. Prabhakaran, N. Parvin, S. Ramakrishna, Thermally-induced two-way shape memory polymers: mechanisms, structures, and applications, Chem. Eng. J. 374 (2019) 706–720, https://doi.org/10.1016/j.cej.2019.05.167.

[6] G. Scalet, S. Pandini, M. Messori, M. Toselli, F. Auricchio, A one-dimensional phenomenological model for the two-way shape-memory effect in semi-crystalline networks, Polymer (guildf) 158 (2018) 130–148, https://doi.org/10.1016/j.polymer.2018.10.027.

[7] N. Inverardi, M. Toselli, G. Scalet, M. Messori, F. Auricchio, S. Pandini, Stress-Free Two-Way Shape Memory Effect of Poly(ethylene glycol)/Poly(ε-caprolactone) Semicrystalline Networks, Macromolecules 55 (2022) 8533–8547, https://doi.org/10.1021/acs.macromol.2c01064.

[8] N. Inverardi, S. Pandini, G. Gemmo, M. Toselli, M. Messori, G. Scalet, F. Auricchio, Reversible Stress-Driven and Stress-Free Two-Way Shape Memory Effect in a Sol-Gel Crosslinked Polycaprolactone, Macromol. Symp. 405 (2022), https://doi.org/10.1002/masy.202100254.

[9] S. Pandini, S. Passera, M. Messori, K. Paderni, M. Toselli, A. Gianoncelli, E. Bontempi, T. Riccò, Two-way reversible shape memory behaviour of crosslinked poly(ε-caprolactone), Polymer (guildf) 53 (2012) 1915–1924, https://doi.org/10.1016/j.polymer.2012.02.053.

[10] D. Ke, Z. Chen, Z.Y. Momo, W. Jiani, C. Xuan, Y. Xiaojie, X. Xueliang, Recent advances of two-way shape memory polymers and four-dimensional printing under stress-free conditions, Smart Mater. Struct. 29 (2020) 023001, https://doi.org/10.1088/1361-665X/ab5e6d.

[11] A. Lendlein, Shape-memory polymers, Springer Berlin, Heidelberg, 2010, https://doi.org/10.1007/978-3-642-12359-7.

[12] A. Lendlein, S. Kelch, Shape-memory polymers, Angew. Chem. Int. Ed. 41 (2002) 2034, https://doi.org/10.1002/1521-3773(20020617)41:12<2034::AID-ANIE2034>3.0.CO;2-M.

[13] X. Wang, Y. He, Y. Liu, J. Leng, Advances in shape memory polymers: Remote actuation, multi-stimuli control, 4D printing and prospective applications, Mater. Sci. Eng. R. Rep. 151 (2022) 100702, https://doi.org/10.1016/j.mser.2022.100702.

[14] F. Momeni, S. M. Mehdi Hassani.N, X. Liu, J. Ni,, A review of 4D printing, Mater Des 122 (2017) 42–79, https://doi.org/10.1016/j.matdes.2017.02.068.

[15] C.M. González-Henríquez, M.A. Sarabia-Vallejos, J. Rodriguez-Hernandez, Polymers for additive manufacturing and 4D-printing: materials, methodologies, and biomedical applications, Prog. Polym. Sci. 94 (2019) 57–116, https://doi.org/10.1016/j.progpolymsci.2019.03.001.

[16] H. Yang, W.R. Leow, T. Wang, J. Wang, J. Yu, K. He, D. Qi, C. Wan, X. Chen, 3D Printed Photoresponsive Devices Based on Shape Memory Composites, Adv. Mater. 29 (2017), https://doi.org/10.1002/adma.201701627.

[17] W. Zhao, F. Zhang, J. Leng, Y. Liu, Personalized 4D printing of bioinspired tracheal scaffold concept based on magnetic stimulated shape memory composites, Compos. Sci. Technol. 184 (2019) 107866, https://doi.org/10.1016/j.compscitech.2019.107866.

[18] Q. Zhang, D. Yan, K. Zhang, G. Hu, Pattern transformation of heat-shrinkable polymer by three-dimensional (3D) printing technique, Sci. Rep. 5 (2015) 8936, https://doi.org/10.1038/srep08936.

[19] W. Liu, N. Wu, K. Pochiraju, Shape recovery characteristics of SiC/C/PLA composite filaments and 3D printed parts, Compos. A Appl. Sci. Manuf. 108 (2018) 1–11, https://doi.org/10.1016/j.compositesa.2018.02.017.

[20] Q. Chen, L. Han, J. Ren, L. Rong, P. Cao, R.C. Advincula, 4D printing via an unconventional fused deposition modeling route to high-performance thermosets, ACS Appl. Mater. Interfaces 12 (2020) 50052–50060, https://doi.org/10.1021/acsami.0c13976.

[21] K. Luo, L. Wang, M.-X. Wang, R. Du, L. Tang, K.-K. Yang, Y.-Z. Wang, 4D Printing of biocompatible scaffolds via *In Situ* photo-crosslinking from shape memory copolyesters, ACS Appl. Mater. Interfaces 15 (2023) 44373–44383, https://doi.org/10.1021/acsami.3c10747.

[22] J.-W. Su, W. Gao, K. Trinh, S.M. Kenderes, E. Tekin Pulatsu, C. Zhang, A. Whittington, M. Lin, J. Lin, 4D printing of polyurethane paint-based composites, Int J Smart Nano Mater 10 (2019) 237–248, https://doi.org/10.1080/19475411.2019.1618409.

[23] X. Wan, F. Zhang, Y. Liu, J. Leng, CNT-based electro-responsive shape memory functionalized 3D printed nanocomposites for liquid sensors, Carbon N Y 155 (2019) 77–87, https://doi.org/10.1016/j.carbon.2019.08.047.

[24] H. Wei, X. Cauchy, I.O. Navas, Y. Abderrafai, K. Chizari, U. Sundararaj, Y. Liu, J. Leng, D. Therriault, Direct 3D printing of hybrid nanofiber-based nanocomposites for highly conductive and shape memory applications, ACS Appl. Mater. Interfaces 11 (2019) 24523–24532, https://doi.org/10.1021/acsami.9b04245.

[25] H. Goodarzi Hosseinabadi, A. Biswas, A. Bhusal, A. Yousefinejad, A. Lall, W. Zimmermann, A.K. Miri, L. Ionov, 4D-printable photocrosslinkable polyurethane-based inks for tissue scaffold and actuator applications, Small (2023), https://doi.org/10.1002/smll.202306387.

[26] Y.Y.C. Choong, S. Maleksaeedi, H. Eng, P.-C. Su, J. Wei, Curing characteristics of shape memory polymers in 3D projection and laser stereolithography, Virtual Phys Prototyp 12 (2017) 77–84, https://doi.org/10.1080/17452759.2016.1254845.

[27] M. Zarek, M. Layani, S. Eliazar, N. Mansour, I. Cooperstein, E. Shukrun, A. Szlar, D. Cohn, S. Magdassi, 4D printing shape memory polymers for dynamic jewellery and fashionwear, Virtual Phys Prototyp 11 (2016) 263–270, https://doi.org/10.1080/17452759.2016.1244085.

[28] H. Wu, P. Chen, C. Yan, C. Cai, Y. Shi, Four-dimensional printing of a novel acrylate-based shape memory polymer using digital light processing, Mater. Des. 171 (2019) 107704, https://doi.org/10.1016/j.matdes.2019.107704.

[29] C. Yang, M. Boorugu, A. Dopp, J. Ren, R. Martin, D. Han, W. Choi, H. Lee, 4D printing reconfigurable, deployable and mechanically tunable metamaterials, Mater. Horiz. 6 (2019) 1244–1250, https://doi.org/10.1039/C9MH00302A.

[30] M. Zarek, M. Layani, I. Cooperstein, E. Sachyani, D. Cohn, S. Magdassi, 3D Printing of Shape Memory Polymers for Flexible Electronic Devices, Adv. Mater. 28 (2016) 4449–4454, https://doi.org/10.1002/adma.201503132.

[31] Y. Wang, E. Sachyani Keneth, A. Kamyshny, G. Scalet, F. Auricchio, S. Magdassi, 4D Multimaterial Printing of Programmable and Selective Light-Activated Shape-Memory Structures with Embedded Gold Nanoparticles, Adv, Mater. Technol. 7 (2022), https://doi.org/10.1002/admt.202101058.

[32] E. Sachyani Keneth, R. Lieberman, M. Rednor, G. Scalet, F. Auricchio, S. Magdassi, Multi-Material 3D Printed Shape Memory Polymer with Tunable Melting and Glass Transition Temperature Activated by Heat or Light, Polymers (basel) 12 (2020) 710, https://doi.org/10.3390/polym12030710.

[33] G. Le Fer, M.L. Becker, 4D Printing of Resorbable Complex Shape-Memory Poly (propylene fumarate) Star Scaffolds, ACS Appl. Mater. Interfaces 12 (2020) 22444–22452, https://doi.org/10.1021/acsami.0c01444.

[34] M. Invernizzi, S. Turri, M. Levi, R. Suriano, Processability of 4D printable modified polycaprolactone with self-healing abilities, Mater. Today:. Proc. 7 (2019) 508–515, https://doi.org/10.1016/j.matpr.2018.12.001.

[35] Y. Zhang, N. Zhang, H. Hingorani, N. Ding, D. Wang, C. Yuan, B. Zhang, G. Gu, Q. Ge, Fast-Response, Stiffness-Tunable Soft Actuator by Hybrid Multimaterial 3D Printing, Adv. Funct. Mater. 29 (2019), https://doi.org/10.1002/adfm.201806698.

[36] Z. Ding, C. Yuan, X. Peng, T. Wang, H.J. Qi, M.L. Dunn, Direct 4D printing via active composite materials, Sci. Adv. 3 (2017), https://doi.org/10.1126/sciadv.1602890.

[37] M. Bodaghi, A.R. Damanpack, W.H. Liao, Adaptive metamaterials by functionally graded 4D printing, Mater. Des. 135 (2017) 26–36, https://doi.org/10.1016/j.matdes.2017.08.069.

[38] M. Bodaghi, A.R. Damanpack, W.H. Liao, Triple shape memory polymers by 4D printing, Smart Mater. Struct. 27 (2018) 065010, https://doi.org/10.1088/1361-665X/aabc2a.

[39] S. Pandini, N. Inverardi, G. Scalet, D. Battini, F. Bignotti, S. Marconi, F. Auricchio, Shape memory response and hierarchical motion capabilities of 4D printed auxetic structures, Mech. Res. Commun. 103 (2020) 103463, https://doi.org/10.1016/j.mechrescom.2019.103463.

[40] N. Inverardi, S. Pandini, F. Bignotti, G. Scalet, S. Marconi, F. Auricchio, Sequential Motion of 4D Printed Photopolymers with Broad Glass Transition, Macromol. Mater. Eng. 305 (2020), https://doi.org/10.1002/mame.201900370.

[41] C. Pasini, N. Inverardi, D. Battini, G. Scalet, S. Marconi, F. Auricchio, S. Pandini, Experimental investigation and modeling of the temperature memory effect in a 4D-printed auxetic structure, Smart Mater. Struct. 31 (2022) 095021, https://doi.org/10.1088/1361-665X/ac8031.

[42] S. Li, Z. Li, S. Mei, X. Chen, B. Ding, Y. Zhang, W. Zhao, X. Zhang, Z. Cui, P. Fu, X. Pang, M. Liu, 4D Printed Thermoplastic Polyamide Elastomers with Reversible Two-Way Shape Memory Effect, Adv Mater Technol 8 (2023), https://doi.org/10.1002/admt.202202066.

[43] D. Chalissery, D. Schönfeld, M. Walter, F. Ziervogel, T. Pretsch, Fused Filament Fabrication of Actuating Objects, Macromol. Mater. Eng. 307 (2022), https://doi.org/10.1002/mame.202200214.

[44] L. Dai, W. Liqian, C. Baihong, X. Zengting, W. Zhijian, X. Rui, Shape memory behaviors of 3D printed liquid crystal elastomers, Soft Science 3 (2023) 4, https://doi.org/10.20517/ss.2022.28.

[45] L. Montesino, J.I. Martínez, C. Sánchez-Somolinos, Reprogrammable 4D Printed Liquid Crystal Elastomer Photoactuators by Means of Light-Reversible Perylene Diimide Radicals, Adv. Funct. Mater. (2023), https://doi.org/10.1002/adfm.202309019.

[46] M. Chen, M. Gao, L. Bai, H. Zheng, H.J. Qi, K. Zhou, Recent Advances in 4D Printing of Liquid Crystal Elastomers, Adv. Mater. 35 (2023), https://doi.org/10.1002/adma.202209566.

[47] H.K. Dave, S.T. Patel, Introduction to Fused Deposition Modeling Based 3D Printing Process, in: 2021: pp. 1–21. doi: 10.1007/978-3-030-68024-4_1.

[48] O.A. Mohamed, S.H. Masood, J.L. Bhowmik, Optimization of fused deposition modeling process parameters: a review of current research and future prospects, Adv. Manuf. 3 (2015) 42–53, https://doi.org/10.1007/s40436-014-0097-7.

[49] E. Malikmammadov, T.E. Tanir, A. Kiziltay, V. Hasirci, N. Hasirci, PCL and PCL-based materials in biomedical applications, J. Biomater. Sci. Polym. Ed. 29 (2018) 863–893, https://doi.org/10.1080/09205063.2017.1394711.

[50] S. Pandini, F. Baldi, K. Paderni, M. Messori, M. Toselli, F. Pilati, A. Gianoncelli, M. Brisotto, E. Bontempi, T. Riccò, One-way and two-way shape memory behaviour of semi-crystalline networks based on sol–gel cross-linked poly (ε-caprolactone), Polymer (guildf) 54 (2013) 4253–4265, https://doi.org/10.1016/j.polymer.2013.06.016.

[51] A. Woern, D. Byard, R. Oakley, M. Fiedler, S. Snabes, J. Pearce, Fused Particle Fabrication 3-D Printing: Recycled Materials' Optimization and Mechanical Properties, Materials 11 (2018) 1413, https://doi.org/10.3390/ma11081413.

[52] M. Messori, M. Degli Esposti, K. Paderni, S. Pandini, S. Passera, T. Riccò, M. Toselli, Chemical and thermomechanical tailoring of the shape memory effect in poly (ε-caprolactone)-based systems, J. Mater. Sci. 48 (2013) 424–440, https://doi.org/10.1007/s10853-012-6757-8.

[53] D. Ribezzi, R. Pinos, L. Bonetti, M. Cellani, F. Barbaglio, C. Scielzo, S. Farè, Design of a novel bioink suitable for the 3D printing of lymphoid cells, Frontiers in Biomaterials Science 2 (2023), https://doi.org/10.3389/fbiom.2023.1081065.

[54] M. Di Giuseppe, N. Law, B. Webb, R.A. Macrae, L.J. Liew, T.B. Sercombe, R. J. Dilley, B.J. Doyle, Mechanical behaviour of alginate-gelatin hydrogels for 3D bioprinting, J. Mech. Behav. Biomed. Mater. 79 (2018) 150–157, https://doi.org/10.1016/j.jmbbm.2017.12.018.

[55] A. Schwab, R. Levato, M. D'Este, S. Piluso, D. Eglin, J. Malda, Printability and Shape Fidelity of Bioinks in 3D Bioprinting, Chem. Rev. 120 (2020) 11028–11055, https://doi.org/10.1021/acs.chemrev.0c00084.

[56] N. Soltan, L. Ning, F. Mohabatpour, P. Papagerakis, X. Chen, Printability and Cell Viability in Bioprinting Alginate Dialdehyde-Gelatin Scaffolds, ACS Biomater Sci. Eng. 5 (2019) 2976–2987, https://doi.org/10.1021/acsbiomaterials.9b00167.

[57] V. Crescenzi, G. Manzini, G. Calzolari, C. Borri, Thermodynamics of fusion of poly-β-propiolactone and poly-ϵ-caprolactone. comparative analysis of the melting of aliphatic polylactone and polyester chains, Eur. Polym. J. 8 (1972) 449–463, https://doi.org/10.1016/0014-3057(72)90109-7.

[58] S. Pandini, S. Agnelli, A. Merlettini, F. Chiellini, C. Gualandi, K. Paderni, M. L. Focarete, M. Messori, M. Toselli, Mutifunctional Electrospun Nonwoven Mats with Two-Way Shape Memory Behavior Prepared from Sol-Gel Crosslinked Poly (ε-Caprolactone), Macromol. Mater. Eng. 302 (2017), https://doi.org/10.1002/mame.201600519.

[59] Ż. Górecka, J. Idaszek, D. Kołbuk, E. Choińska, A. Chlanda, W. Święszkowski, The effect of diameter of fibre on formation of hydrogen bonds and mechanical properties of 3D-printed PCL, Mater. Sci. Eng. C 114 (2020) 111072, https://doi.org/10.1016/j.msec.2020.111072.

[60] M. Kempfert, E. Willbold, S. Loewner, C. Blume, J. Pitts, H. Menzel, Y. Roger, A. Hoffmann, N. Angrisani, J. Reifenrath, Polycaprolactone-Based 3D-Printed Scaffolds as Potential Implant Materials for Tendon-Defect Repair, J Funct Biomater 13 (2022) 160, https://doi.org/10.3390/jfb13040160.

[61] W. Liu, Z. Feng, W. Ou-Yang, X. Pan, X. Wang, P. Huang, C. Zhang, D. Kong, W. Wang, 3D printing of implantable elastic PLCL copolymer scaffolds, Soft Matter 16 (2020) 2141–2148, https://doi.org/10.1039/C9SM02396H.

[62] C. O'Connell, J. Ren, L. Pope, Y. Zhang, A. Mohandas, R. Blanchard, S. Duchi, C. Onofrillo, Characterizing Bioinks for Extrusion Bioprinting, Printability and Rheology, in (2020:) 111–133, https://doi.org/10.1007/978-1-0716-0520-2_7.

[63] I. Razquin, A. Iregui, M. Cobos, J. Latasa, A. Eceiza, K. González, L. Martin, A. J. Müller, A. González, L. Irusta, Cationically photocured epoxy/polycaprolactone materials processed by solution electrospinning, melt electrowriting and 3D printing: Morphology and shape memory properties, Polymer (guildf) 282 (2023) 126160, https://doi.org/10.1016/j.polymer.2023.126160.

[64] S. Pandini, D. Dioni, K. Paderni, M. Messori, M. Toselli, E. Bontempi, T. Riccò, The two-way shape memory behaviour of crosslinked poly(ε-caprolactone) systems with largely varied network density, J. Intell. Mater. Syst. Struct. 27 (2016) 1388–1403, https://doi.org/10.1177/1045389X15591384.

[65] S. Pandini, T. Riccò, A. Borboni, I. Bodini, D. Vetturi, D. Cambiaghi, M. Toselli, K. Paderni, M. Messori, F. Pilati, F. Chiellini, C. Bartoli, Tailored One-Way and Two-Way Shape Memory Capabilities of Poly(ε-Caprolactone)-Based Systems for Biomedical Applications, J. Mater. Eng. Perform. 23 (2014) 2545–2552, https://doi.org/10.1007/s11665-014-1033-5.

[66] T. Chung, A. Romo-Uribe, P.T. Mather, Two-Way Reversible Shape Memory in a Semicrystalline Network, Macromolecules 41 (2008) 184–192, https://doi.org/10.1021/ma071517z.

[67] The mechanics of two-dimensional cellular materials, Proceedings of the Royal Society of London. A. Mathematical and Physical Sciences 382 (1982) 25–42. doi: 10.1098/rspa.1982.0087.

[68] Y. Kim, K.H. Son, J.W. Lee, Auxetic Structures for Tissue Engineering Scaffolds and Biomedical Devices, Materials 14 (2021) 6821, https://doi.org/10.3390/ma14226821.

[69] Q. Ge, A.H. Sakhaei, H. Lee, C.K. Dunn, N.X. Fang, M.L. Dunn, Multimaterial 4D Printing with Tailorable Shape Memory Polymers, Sci. Rep. 6 (2016) 31110, https://doi.org/10.1038/srep31110.

[70] T.G. Leong, C.L. Randall, B.R. Benson, N. Bassik, G.M. Stern, D.H. Gracias, Tetherless thermobiochemically actuated microgrippers, in: Proceedings of the National Academy of Sciences 106, 2009, pp. 703–708, https://doi.org/10.1073/pnas.0807698106.

[71] H. Du, J. Zhang, Solvent induced shape recovery of shape memory polymer based on chemically cross-linked poly(vinyl alcohol), Soft Matter 6 (2010) 3370, https://doi.org/10.1039/b922220k.

[72] K. Uto, T. Aoyagi, C.A. DeForest, A.S. Hoffman, M. Ebara, A Combinational Effect of "Bulk" and "Surface" Shape-Memory Transitions on the Regulation of Cell Alignment, Adv. Healthc. Mater. 6 (2017), https://doi.org/10.1002/adhm.201601439.

[73] X. Liu, K. Zhao, T. Gong, J. Song, C. Bao, E. Luo, J. Weng, S. Zhou, Delivery of Growth Factors Using a Smart Porous Nanocomposite Scaffold to Repair a Mandibular Bone Defect, Biomacromolecules 15 (2014) 1019–1030, https://doi.org/10.1021/bm401911p.

[74] I. Apsite, J.M. Uribe, A.F. Posada, S. Rosenfeldt, S. Salehi, L. Ionov, 4D biofabrication of skeletal muscle microtissues, Biofabrication 12 (2020) 015016, https://doi.org/10.1088/1758-5090/ab4cc4.

[75] C.-S. Yang, H.-C. Wu, J.-S. Sun, H.-M. Hsiao, T.-W. Wang, Thermo-Induced Shape-Memory PEG-PCL Copolymer as a Dual-Drug-Eluting Biodegradable Stent, ACS Appl. Mater. Interfaces 5 (2013) 10985–10994, https://doi.org/10.1021/am4032295.

[76] F. Causa, E. Battista, R. Della Moglie, D. Guarnieri, M. Iannone, P.A. Netti, Surface Investigation on Biomimetic Materials to Control Cell Adhesion: The Case of RGD Conjugation on PCL, Langmuir 26 (2010) 9875–9884, https://doi.org/10.1021/la100207q.

[77] N. Recek, M. Resnik, H. Motaln, T. Lah-Turnšek, R. Augustine, N. Kalarikkal, S. Thomas, M. Mozetič, Cell Adhesion on Polycaprolactone Modified by Plasma Treatment, Int J Polym Sci 2016 (2016) 1–9, https://doi.org/10.1155/2016/7354396.

[78] T. Patrício, M. Domingos, A. Gloria, P. Bártolo, Characterisation of PCL and PCL/PLA Scaffolds for Tissue Engineering, Procedia CIRP 5 (2013) 110–114, https://doi.org/10.1016/j.procir.2013.01.022.

[79] A. Kumar, S.M. Mir, I. Aldulijan, A. Mahajan, A. Anwar, C.H. Leon, A. Terracciano, X. Zhao, T. Su, D.M. Kalyon, S.G. Kumbar, X. Yu, Load-bearing biodegradable PCL-PGA-beta TCP scaffolds for bone tissue regeneration, J. Biomed. Mater. Res. B Appl. Biomater. 109 (2021) 193–200, https://doi.org/10.1002/jbm.b.34691.